Ensemble forecast of an index of the Madden Julian Oscillation using a stochastic weather generator based on circulation analogs

Meriem Krouma [1,2], Riccardo Silini [3], and Pascal Yiou [2]

[1]ARIA Technologies, 8 Rue de la Ferme, 92100 Boulogne-Billancourt, France.
[2]Laboratoire des Sciences du Climat et de l'Environnement, UMR 8212 CEA-CNRS-UVSQ, IPSL & Université Paris-Saclay, 91191 Gif-sur-Yvette, France.
[3]Departament de Fisica, Universitat Politècnica de Catalunya, Edifici Gaia, Rambla Sant Nebridi 22, 08222 Terrassa, Barcelona, Spain.

Correspondence: Meriem Krouma (meriem.krouma@lsce.ipsl.fr)

Abstract.

The Madden-Julian Oscillation (MJO) is one of the main sources of sub-seasonal atmospheric predictability in the Tropical region. The MJO affects precipitation over highly populated areas, especially around Southern India. Therefore, predicting its phase and intensity is important as it has a high societal impact. Indices of the MJO can be derived from the first principal
5 components of wind speed and outgoing longwave radiation (OLR) in the Tropics (RMM1 and RMM2 indices). The amplitude and phase of the MJO are derived from those indices. Our goal is to forecast these two indices on a sub-seasonal timescale. This study aims to provide an ensemble forecast of MJO indices from analogs of the atmospheric circulation, computed from the geopotential at 500 hPa (Z500) by using a stochastic weather generator (SWG). We generate an ensemble of 100 members for the MJO amplitude for sub-seasonal lead times (from 2 to 4 weeks). Then we evaluate the skill of the ensemble forecast
10 and the ensemble mean using probabilistic scores and deterministic skill scores. According to score-based criteria, we find that a reasonable forecast of the MJO index could be achieved within 40-day lead times for the different seasons. We compare our SWG forecast with other forecasts of the MJO.

1 Introduction

Forecasting the Madden Julian Oscillation (MJO) is a crucial scientific endeavor as the MJO represents one of the most
15 important sources of subseasonal predictability in the tropics. The Madden Julian oscillation controls tropical convection, with a life cycle going from 30 to 60 days (Lin et al., 2008). It is characterized by a dominant eastward propagation over the tropical Indo-Pacific basin in particular during the boreal winter. The MJO affects the Indian, Australian monsoons (Zhang, 2013), and West African monsoon (Barlow et al., 2016). It was shown that it affects precipitation in East Asia (Zhang et al., 2013) and North America (Becker et al., 2011). The MJO affects the global weather as it impacts the tropics as well as the extratropics
20 due to the atmospheric teleconnections (Zhang, 2013; Cassou, 2008).

The improvement of the forecast skill of the MJO is subject of several studies. Numerical models have shown an ability to forecast the MJO index (Kim et al., 2018). However, the forecast of the MJO is sensitive to the quality of the initial conditions

(Zhang, 2013; Straub, 2013). This motivates probabilistic forecasts to overcome the chaotic nature of climate variability (Sivillo et al., 1997; Palmer, 2000). Indeed, ensemble forecasts have shown improvements over deterministic forecasts for weather and climatic variables on short and long term (Yiou and Déandréis, 2019; Hersbach et al., 2020). One of the advantages of ensemble forecasts is that they provide information about the forecast uncertainties, which deterministic forecasts cannot provide. In addition, the use of ensemble means has shown better forecast results than the individual ensemble members in previous works (Toth and Kalnay, 1997; Grimit and Mass, 2002; Xiang et al., 2015).

Statistical models, such as stochastic weather generators (SWG), have been used for this purposes. SWGs are designed to mimic the behavior of climate variables (Ailliot et al., 2015). They have been used to forecast various weather and climatic variables such as temperature (Yiou and Déandréis, 2019), precipitation (Krouma et al., 2021) and the North Atlantic oscillation (NAO) (Yiou and Déandréis, 2019). One of the benefits of using stochastic weather generators is that they have a low computing cost compared to numerical models. Combining stochastic weather generators with analogs of the atmospheric circulation is an efficient approach to generate ensemble weather forecasts with consistent atmospheric patterns (Yiou and Déandréis, 2019; Krouma et al., 2021; Blanchet et al., 2018).

Analogs of circulation were designed to provide forecast assuming that similar situations in the atmospheric circulation could lead to similar local weather conditions (Lorenz, 1969). Recent studies have evaluated the potential of analogs to forecast the probability distribution of climate variables: Yiou and Déandréis (2019) simulated large ensemble members of temperature using random sampling of atmospheric circulation analogs; Atencia and Zawadzki (2014) used analogs of precipitation to forecast precipitation.

The goal of this study is to forecast a daily MJO index for a subseasonal lead time ($\approx 2 - 4$ weeks) with a SWG based on analogs of the atmospheric circulation, described in Sec. 3.2. The SWG approach was evaluated in previous studies by Yiou and Déandréis (2019) and Krouma et al. (2021) for European temperature and precipitation. The SWG was able to forecast the temperature within 40 days and the precipitation within 20 days with reasonable skill scores in western Europe (Krouma et al., 2021; Yiou and Déandréis, 2019). In this paper, we adjust the parameters of the SWG in order to forecast the MJO indices. More precisely, our goals are (i) to forecast the MJO amplitude (directly from the amplitude, and using the MJO indices), and (ii) to evaluate the ability of our SWG model to forecast active events of the MJO for the following weeks. We will evaluate the sensitivity of the SWG approach on the forecast with different seasons and compare the forecast skill using SWG to other forecast approaches.

The paper is divided as follows: Section 2 shows the data used for running our forecast. Section 3 explains the methodology: circulation analogs, stochastic weather generator and the verification metrics that we used to evaluate the SWG forecast. Section 4 explains the experimental setup. Section 5 details results of simulations and the evaluation of the ensemble forecast. Section 6 is devoted to the comparison of the SWG forecast with the literature. Section 7 contains the main conclusions of the analyses.

2 Data

55   The MJO has been described by various indices, that are obtained from different atmospheric variables (Stachnik and Chrisler, 2020). Wheeler and Hendon (2004) defined an MJO index from two so-called Real-time Multivariate MJO series (RMM). RMM1 and RMM2 represent respectively the first and second principal components of the empirical orthogonal functions (EOFs) resulting from the combination of daily fields of the satellite-observed outgoing longwave radiation (OLR), and the zonal wind at 250 hPa and 850 hPa latitudinally averaged between 15°N and 15°S (Rashid et al., 2011). The EOFs are computed

60   from daily normalized fields after applying a filter to remove the long timescale variability (annual mean and the first three harmonics of the seasonal cycle), the previous 120 days of anomaly fields and the El Niño signal as described by Wheeler and Hendon (2004). Lim et al. (2018) and Ventrice et al. (2013) proposed other indices proposed of the MJO. The main difference between the indices consists in the input fields and the computation of the index. For instance, Ventrice et al. (2013) replace OLR with 200hPa velocity potential and Lim et al. (2018) do not remove an El Niño signal.

65   For this paper, we selected the RMM-based MJO index of The RMM1 and RMM2 allow to compute the amplitude and the phase of the MJO Wheeler and Hendon (2004). One of the reasons is that it is often used for MJO forecast (e.g. Kim et al., 2018; Rashid et al., 2011; Silini et al., 2021).

To simplify notations in the equations, we will note $R_1 = \mathrm{RMM1}$ and $R_2 = \mathrm{RMM2}$. The amplitude (A) and phase (ϕ) are defined as follows:

70
$$A(t) = \sqrt{R_1(t)^2 + R_2(t)^2}, \tag{1}$$

and

$$\phi(t) = \tan^{-1}\frac{R_2(t)}{R_1(t)}. \tag{2}$$

The amplitude and the phase describe respectively the evolution of the MJO and its position along the equator. The amplitude is related to the intensity of the MJO activity. For instance, we consider that there is a MJO event when $A(t) \geq 1$. There are

75   different classifications related to the intensity of the active MJO events (Lafleur et al., 2015). The phase ϕ is decomposed into eight areas known as centers of convection of the MJO over the equator, starting from the Indian Ocean through the maritime continent to the western Pacific Ocean. This leads to a discretization $\hat{\phi}$ of phase ϕ into those eight identified areas (Lafleur et al., 2015). For each day t, we consider the amplitude $A(t)$, which can be above 1 (active MJO) or below 1, and the phase $\hat{\phi} \in \{1, \ldots, 8\}$. The amplitude and the phase are usually represented in a phase-space diagram (Lafleur et al., 2015), called the

80   Wheeler-Hendon phase diagram. An example of Wheeler-Hendon phase diagram is shown in Figure 1.

We obtained daily time series of RMMs, amplitude (A) and phase ($\hat{\phi}$) from January 1979 to December 2020 over the region covering 15°N – 15°S, from the University of Columbia (USA) (Wheeler and Hendon, 2004). In this paper, we aim at forecasting RMM variations.

We used the geopotential at 500 hPa (Z500), 300 hPa (Z300) and Outgoing Longwave Radiation (OLR) daily data to compute
85 the analogs. The data are available from 1948 to 2020 with a horizontal resolution of $2.5° \times 2.5°$. The data were downloaded
from the National Centers for Environmental Prediction (NCEP, Kistler et al. (2001)).

In this paper, we predict the daily amplitude A and phase ϕ of the MJO, from the daily analogs of Z500, Z300 and OLR.
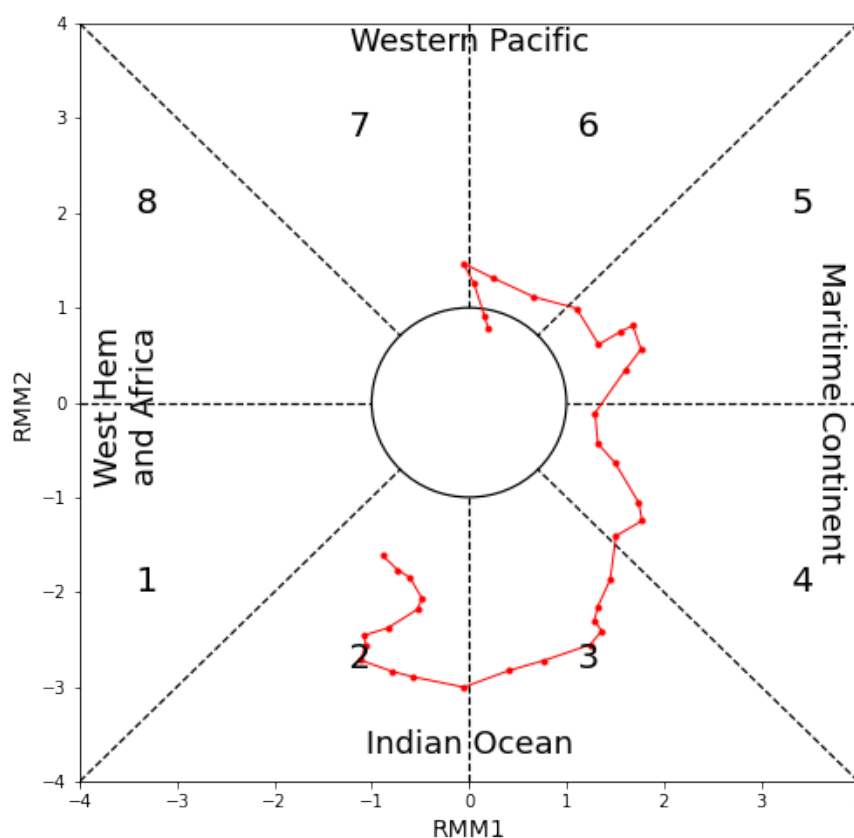
Figure 1. Wheeler-Hendon phase diagram of the MJO event for the period between 1986/03/03 and 1986/04/09, for observations. The
Diagram shows the 8 areas of activity of MJO starting from the Indian Ocean.

4

3 Methodology

3.1 Analog computation

90 We start by building a database of analogs. For a day t, we define analogs as dates t' within 30 calendar days of t that have a similar Z500 (or Z300 or OLR) configuration as t. We look for analogs in different years from t. We quantify the similarity between daily Z500 maps using the Euclidean distance. The analogs are computed from daily data using a moving time window of $\Delta = 30$ days. This duration Δ corresponds to the life cycle of the MJO. Then, we keep the 20 best analogs. We define "best analog" as dates which have the minimum Euclidean distance between t and t'. The use of the Euclidean distance and the

95 number of the analogs were explored and justified in previous studies (Krouma et al., 2021; Platzer et al., 2021).

Hence the distance that is optimized to find analogs of the $Z500(x,t)$ field is:

$$D(t,t') = \left[\sum_x \left(\sum_{i=0}^{\tau} |Z500(x,t+i) - Z500(x,t'+i)|^2 \right) \right]^{\frac{1}{2}}, \tag{3}$$

where x is a spatial index, τ is a time window size (e.g. $\tau = 3$ days).

We compute separately analogs of Z500, Z300 and OLR following the same procedure over the Indian Ocean as represented

100 in Figure 2. We explored different ways to compute the analogs mainly the search window of the analogs and the adjustment of the geographical domain. We considered different geographical regions to search for analogs. We computed analogs over the Indian ocean, the Indian-Pacific ocean and the Indian-maritime ocean for verification purposes (Annex B1). This lead to consider an optimal region for the analog search outlined in Figure 2.
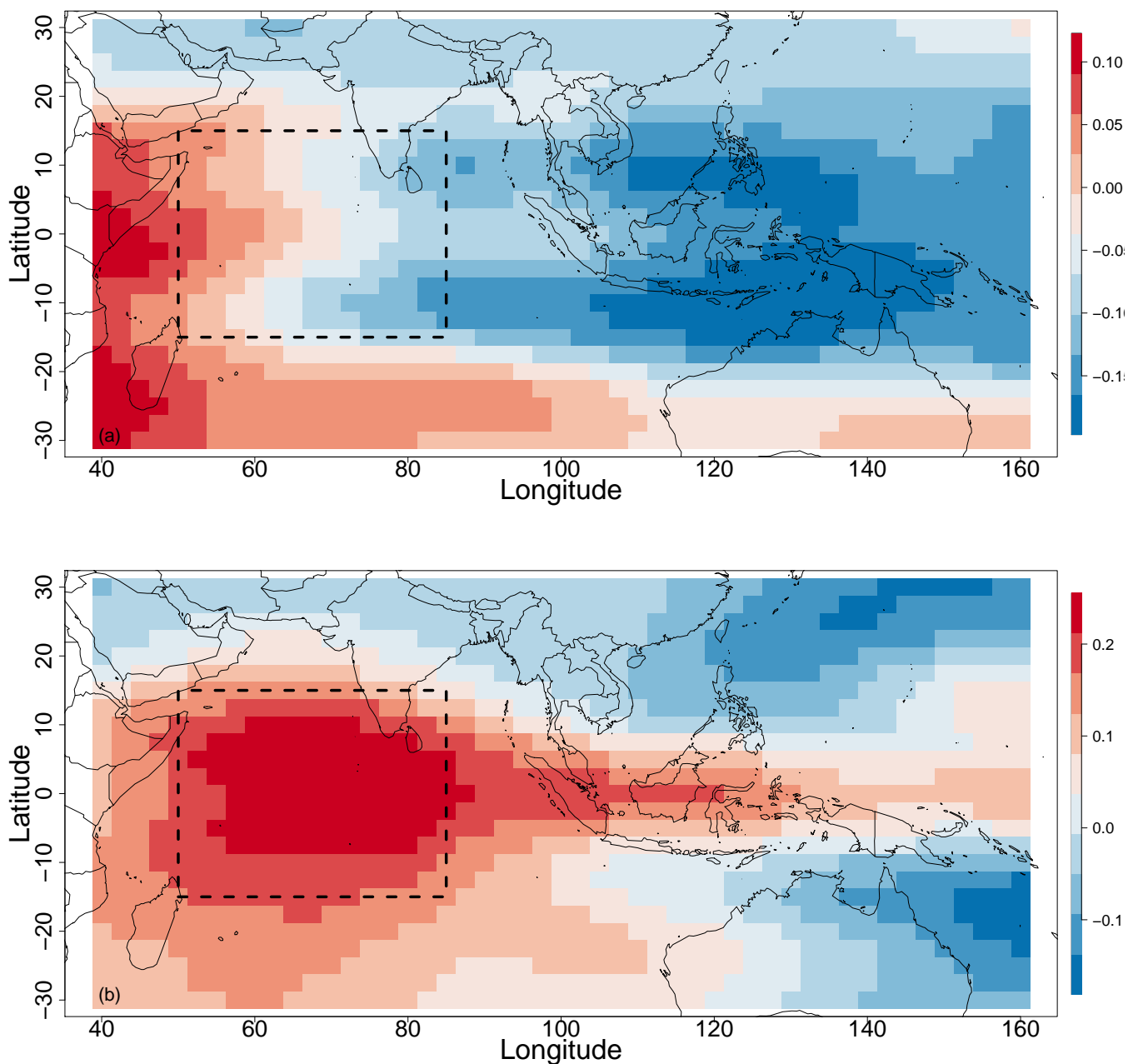
Figure 2. The optimal domain of computation of analogs, we computed analogs over the Indian ocean, in the geographic areas indicated by the black dash rectangle with coordinates (50E – 85E; 15S – 15N). The figure shows the temporal correlation between Z500, RMM1 (panel a) and RMM2 (panel b) for the whole studied period from 1979 to 2020. The correlation is weak but it is still significant (with p-values ≤ 0.05) for the indicated domain.

3.2 Configuration of the stochastic weather generator

The purpose of the stochastic weather generator (SWG) is to generate ensembles of random trajectories that yield physically consistent features. The SWG we use is based on circulation analogs that are computed in advance with the procedure described in Section 3.1 (Yiou, 2014; Krouma et al., 2021). We produce an ensemble hindcast forecast with the circulation analog SWG with the following procedure. For a given day t_0 in year y_0, we generate a set of $S = 100$ simulations until a time $t_0 + T$, where T is the lead time, that goes from 3 to 90 days. We start at day t_0 and randomly select an analog (out of $K = 20$) of day $t_0 + 1$. The random selection of analogs of day $t_0 + 1$ among K analogs is performed with weights w_k that are computed are the products of two weights w_k^c and w_k^ϕ defined by the following rules:

1. weights w_k^c are inversely proportional to the calendar difference between t_0 and analog dates, to ensure that time goes "forward". If δ_k is the difference of calendar days between $t_0 + 1$ and the kth analogue of $t_0 + 1$, then the calendar day sampling weight w_k^c is proportional to $\exp(-|\delta_k|)$.

2. More weight is given to analogs which are in the same phase. If δ'_k is the difference between $\hat{\phi}(t_0 + 1)$ and the discrete phase $\hat{\phi}_k$ of the kth analog, then the phase weight w_k^ϕ is proportional to $\exp(-|\delta'_k|)$.

Then we set $w_k = 0$ when the analog year is y_0. Indeed, excluding analog selection in year y_0, ensures that we do not use information from the T days that follow t_0. Then $w_k = w_k^c \times w_k^\phi$ and the values of w_k are normalized so that their sum is 1. The rules 1 is similar to the SWG used by Krouma et al. (2021). Rule 2 adds a constraint to ensure a phase consistence across analogs.

We then replace t_0 by the selected analog of $t_0 + 1$ and repeat the operation T times. Hence we obtain a hindcast trajectory between t_0 and $t_0 + T$. This operation of trajectory simulation from t_0 to $t_0 + T$ is repeated $S = 100$ times. The daily MJO ($A(t)$ or RMMs) of each trajectory is time-averaged between t_0 and $t_0 + T$. Hence, we obtain an ensemble of $S = 100$ forecasts of the average MJO ($A(t)$ or RMMs) for day t_0 and lead time T. Then t_0 is shifted by $\Delta t \geq 1$ days, and the ensemble simulation procedure is repeated. This provides a set of ensemble forecasts with analogs.

To evaluate our forecasts, the predictions made with the SWG are compared to the persistence and climatological forecasts. The persistence forecast consists of using the average value between $t_0 - T$ and t_0 for a given year. The climatological forecast takes the climatological mean between t_0 and $t_0 + T$. The persistence and climatological forecasts are randomized by adding a small Gaussian noise, whose standard deviation is estimated by bootstrapping over T long intervals. We thus generate sets of persistence forecasts and climatological forecasts that are consistent with the observations (Yiou and Déandréis, 2019).

3.3 Forecast verification metrics

We assess the skill of the SWG to forecast the $A(t)$ and the RMMs using two approaches. We start by evaluating the performance of the SWG to forecast $A(t)$. For that, we use probabilistic scores (Zamo and Naveau, 2018; Hersbach, 2000; Marshall et al., 2016), like the Continuous Rank probability Score (CRPS) for each lead time T. The CRPS is a quadratic measure of

135 the difference between the forecast cumulative distribution function and the empirical cumulative distribution function of the observation (Zamo and Naveau, 2018). The CRPS is defined by:

$$CRPS(P, x_a) = \int\limits_{-\infty}^{+\infty} (P(x) - \mathcal{H}(x - x_a))^2 dx, \tag{4}$$

where x_a is the observed RMM^{obs} or $A(t)^{obs}$, P is the cumulative distribution function of x of the ensemble forecast and $\mathcal{H}$ represents the Heaviside function, ($\mathcal{H}(y) = 1$ if $y \geq 0$, and $\mathcal{H}(y) = 0$ otherwise). A perfect forecast yields a CRPS value equal

140 to 0.

As the CRPS value depends on the unit of the variable to be predicted, it is useful to normalize it with the CRPS value of a reference forecast, which can be obtained by a persistence or a climatology hypothesis. The CRPSS is defined as a percentage of improvement over such a reference forecast (Hersbach, 2000). We compute the CRPSS using as a reference the climatology and the persistence.

145 $$CRPSS = 1 - \frac{\overline{CRPS}}{\overline{CRPS_{ref}}}, \tag{5}$$

where $\overline{CRPS}$ is the average of the $CRPS$ of the SWG forecast and $\overline{CRPS_{ref}}$ is the average of the $CRPS$ of the reference (either climatology or persistence).

The CRPSS values vary between $-\infty$ and 1. The forecast has improvement over the reference when the CRPSS value is above 0.

150 We also computed the rank (temporal) correlation between the observations and the median of the 100 simulations (Scaife et al., 2014).

A robust forecast requires a good discrimination skill. A discrimination skill represents the ability to distinguish events from non-events. We measure the skill of the SWG in discriminating between situations leading to the occurrence of an MJO event (active MJO) and those leading to the non-occurrence of the event (inactive MJO). To do so, we use the relative operating

155 characteristic (ROC) score. The ROC is used for binary events (Fawcett, 2006). Since we have a probabilistic forecast, we can use a threshold value of 1 to construct a classifier for the binary event of MJO from the feature $A(t)$:

– If $A(t) \geq 1$ we predict a positive outcome (active MJO),

– if $A(t) < 1$ we predict a negative outcome (inactive MJO).

The ROC curve is a plot of the success rate versus the false alarm rate (Verde, 2006). The ROC curve could be also a plot

160 of the *sensitivity* versus the *specificity* (Fawcett, 2006). The sensitivity (true positive rate) is the probability of an active MJO event, assuming that $A(t) \geq 1$ is really observed. The specificity (true negative rate), refers to the probability of an inactive MJO event, as long as we have $A(t) \leq 1$. Moreover, the sensitivity is a measure of the ability of the prediction to identify true positives and the specificity is a measure of the ability to identify true negatives. Both quantities describe the accuracy of a

prediction that signals the presence or absence of a MJO event (Fawcett, 2006). Therefore, we define the relationship between

165 sensitivity and specificity as follow:

- $specificity = 1 - sensitivity$ means that we have a poor prediction because the rate of true negative and the false alarm rate are the same,

- $specificity > 1 - sensitivity$ means that we have a good prediction.

Another performance measurement that we can infer from the ROC curve is the Area Under the Curve (AUC). The AUC

170 explains how much the forecast model is able to distinguish between binary classes. The AUC is the area in the ROC curve between sensitivity and the false positive rate computed as follow:

$$AUC = \int_0^1 S(x)dx \tag{6}$$

Where S is the sensitivity and x is the false positive rate.

An increase in AUC indicates an improvement in discriminatory abilities of the model at predicting a negative outcome as a

175 negative outcome and a positive outcome as a positive outcome. An AUC of 0.5 is non-informative.

Finally, we evaluate the ensemble mean forecast of $RMM1$ and $RMM2$ using the usual scalar metrics for MJO forecast (Rashid et al., 2011; Silini et al., 2021; Kim et al., 2018). We computed the bivariate anomaly correlation coefficient (COR) and the bivariate root mean square error (RMSE) between the forecasted RMMs (R_i^{pred}) and the observed RMMs (R_i^{obs}) as follow:

180 $$COR(T) = \frac{\sum_{t=1}^{t=N}[R_1^{obs}(t)R_1^{pred}(t,T) + R_2^{obs}(t)R_2^{pred}(t,T)]}{\sqrt{\sum_{t=1}^{t=N}[R_1^{obs}(t)^2 + R_2^{obs}(t)^2]}\sqrt{\sum_{t=1}^{N}[R_1^{pred}(t,T)^2 + R_2^{pred}(t,T)^2]}}, \tag{7}$$

$$RMSE(T) = \sqrt{\frac{\sum_{t=1}^{t=N}[|R_1^{obs}(t) - R_1^{pred}(t,T)|^2 + |R_2^{obs}(t) - R_2^{pred}(t,T)|^2]}{N}}, \tag{8}$$

where t is the time, T is the lead time of the forecast, N is the length of the time series ($N \sim 10^4$). We interpret the values of COR and RMSE using thresholds fixed by previous studies to define the forecast skill of the SWG. The forecast has skill when the COR value is larger than 0.5 and the RMSE value is lower than $\sqrt{2}$. Rashid et al. (2011) explain that for a climatological

185 forecast, $RMSE = \sqrt{2}$ because the standard deviation of the observed RMM indices is 1. Hence, forecasts are considered to be skilful for $RMSE < \sqrt{2}$ (i.e., they have lower RSME than a climatological forecast). We will use those threshold in our analyses.

We compare the RMSE to the ensemble spread in order to evaluate the forecast accuracy. The ensemble spread measures the difference between the members of the ensemble forecast. The ensemble spread ES is obtained by the root mean square

190 difference between the ensemble members and the ensemble mean defined as follow:

$$ES = \sqrt{\frac{\sum_{n=1}^{S}(A_n - \overline{A})^2}{S}}, \tag{9}$$

where S is the size of the ensemble members, A_n is the amplitude of the nth ensemble member of the forecast and $\hat{A}$ is the ensemble average of A_n over the S members.

We compute the average amplitude error (E_A) and the average phase error (E_ϕ) for the different lead times T. They allow to evaluate the quality of the forecast. The average amplitude error (E_A) is defined as follow:

$$E_{A(T)} = \frac{1}{N} \sum_{t=1}^{t=N} [A_{pred}(t,T) - A_{obs}(t)], \tag{10}$$

The value of $E_{A(T)}$ indicates how fast the forecast system loses the amplitude of the MJO signal. If a positive value indicates an overestimation of the amplitude in predictions compared to the observation. A negative value indicates an underestimated amplitude. Rashid et al. (2011) define the average phase error (E_ϕ) as:

$$E_{\phi(T)} = \frac{1}{N} \sum_{t=1}^{t=N} \tan^{-1} \frac{R_1^{obs}(t)R_2^{pred}(t,T) - R_2^{obs}(t)R_1^{pred}(t,T)}{R_1^{obs}(t)R_1^{pred}(t,T) + R_2^{obs}(t)R_2^{pred}(t,T)}. \tag{11}$$

This formulation stems from the ratio of the cross product (numerator) and dot product (denominator) of the vectors of forecast (R_1^{pred}, R_2^{pred}) and observations (R_1^{obs}, R_2^{obs}). Eq. (11) is equivalent to the average phase angle difference between the prediction and observations, with a positive angle indicating the forecast leads the observations (Rashid et al., 2011). The negative (positive) value of $E_{\phi(T)}$ indicates a slower (faster) propagation of the phase in predictions compared to the observations.

4 Forecast Protocol

We explore the skill of a SWG to forecast the $A(t)$ and the $RMMs$ (R_1 and R_2) using analogs of the atmospheric circulation. We generate separately an ensemble of 100 members of the $A(t)$ of the MJO and RMMs using the same approach. The goal is to have a probabilistic forecast of the $A(t)$ for a subseasonal lead time T ($\approx$ 2 to 4 weeks). As input to the SWG, we are using analogs of the atmospheric circulations. We computed analogs separately from Z500, Z300 and the OLR. And we choose to keep analogs from the geopotential at height 500 hPa instead of the fields OLR or Z300. One reason of this choice is based on the composition of the RMMs index. Indeed, the OLR is used as a proxy for organized moist convection. However, the fractional contribution of the convection to the variance of RMMs is considerably lower than the fraction of the zonal wind fields (Kim et al., 2018; Straub, 2013).

Then, we adjusted the geographical region and the window search of analogs. Indeed, the forecast skill of the MJO depends on the geographical region. We choose to compute the analogs over the Indian Ocean with coordinates (50°E − 85°E; 15°S −15°N). We argued our choice by the fact that (i) the Indian Ocean corresponds to the first phase of the MJO in the phase-space diagram, where the MJO starts. (ii) Different models found good results by initiating their forecast in this region (Kim et al., 2018).

We search for analogs within 30 calendar days. This duration corresponds to the life cycle of the MJO. In addition, we adjust the SWG in order to select analogs from the same phase, as described in Section 3.2.

To evaluate the skill score of our forecasts, we used two approaches. We used the probabilistic scores such as CRPS, correlation and ROC score (section 3.3) to evaluate the ensemble forecast of the amplitude. Then, we evaluate the ensembles mean of $RMM1$ and $RMM2$. For that, we used scalar metrics such as the COR and the RMSE (section 3.3), as they are

225   commonly used to evaluate MJO forecast (Rashid et al., 2011; Lim et al., 2018).

5 Results

We show the results of the forecast of $A(t)$ and $RMMs$ (R_1 and R_2) from the analogs of Z500 over the Indian Ocean with a time of search of 30 days. As explained in section 4, we explored the potential of other atmospheric circulations (OLR and Z300) to forecast the MJO amplitude. However, the forecast skill using analogs of OLR were not that satisfying compared to

230   the Z500 (Annexes: Figures A4). This could be explained by the fact that the MJO predictability can be improved by including atmospheric and oceanic process (Pegion and Kirtman, 2008).

We also tested the forecast of A(t) and RMMs using analogs of Z300. We get good forecast skill (i.e. with $COR > 0.5$ and $RMSE < \sqrt{2}$) up to $T = 60$ days. However, we notice that the forecast skill scores based on analogs of Z500 are higher for small lead times (up to 30 days). The results of the forecast with analogs of Z300 could be found in the annexes (A1 to A3). For

235   those reasons, we decided to keep results of the forecast for $A(t)$ and RMMs with analogs of Z500. Therefore, this highlights the capacity of Z500 to catch the variability of the MJO.

For an illustration, we show the time series of the simulations and observations of the MJO amplitude for 1986. This year yields an unusually large period of RMM amplitude above 1, suggesting an important MJO activity. Figure 3 shows the mean of the 100 simulations and the observations for lead times of 3, 5 and 10 days for the whole year. We find that there is a strong

240   correlation between observed and simulated $A(t)$ for the different lead times represented. Moreover, the SWG was able to distinguish between the active MJO days ($A(t) \geq 1$) and inactive MJO ($A(t) < 1$).
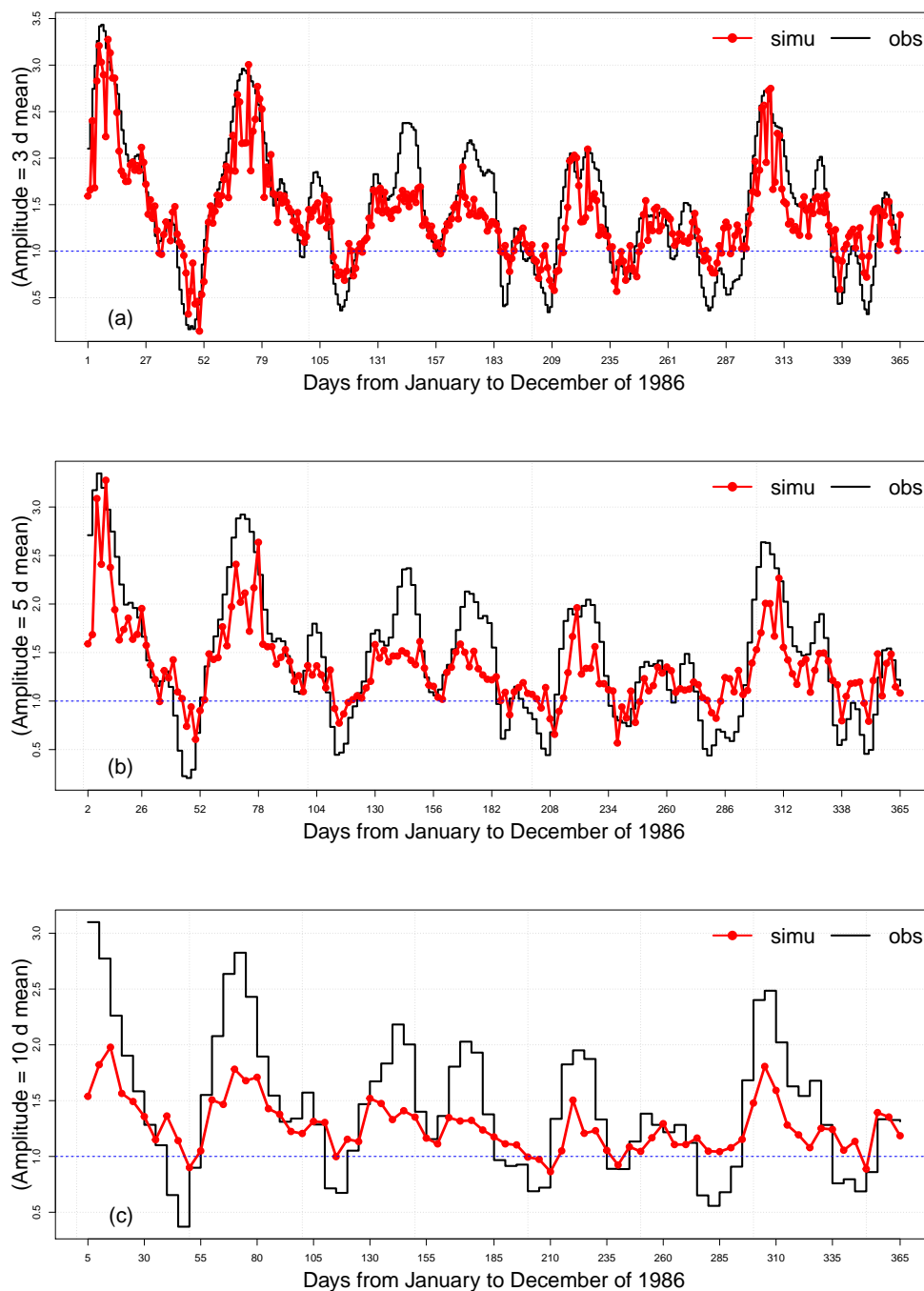
Figure 3. Time series of observations and simulations of the MJO Amplitude for lead time of 3, 5 and 10 days, respectively (a), (b) and (c), for the year 1986. The red line represents the mean of the 100 simulations, the black line represents the observations, and the blue line indicates the threshold of the MJO activity (below 1: inactive; above 1: active)

5.1 Evaluation of the Ensemble forecast of the MJO Amplitude

We evaluate the forecast of amplitude $A(t)$ using the probabilistic skill scores (CRPSS, ROC and correlation) defined in Section 3.3. We are considering the average of the skill scores up to each lead time T. In Figure 4, we show the CRPSS and the

245　correlation for DJF (December, January and February) and JJA (June, July and August) for different lead times T going from 3 to 40 days.

The CRPSS was computed using as a reference the forecast made from climatology and persistence. We notice that the CRPSS vs. persistence reference is decreasing with time. It has higher values for $T = 3, 5, 10$ days. We notice that when the lead time is larger than $T = 15$ days, CRPSS values become stable for both seasons. However, the CRPSS vs. climatology

250　is increasing with lead times. We notice that for small lead times ($T \leq 15$ days), the SWG forecast is doing better than the persistence, while for big lead times $T \geq 15$ days, the SWG forecast is doing better than the climatology. We can say that the forecast has positive improvement compared to climatology and persistence for DJF and JJA for all the studied lead times. We see that correlation is mostly decreasing with lead times. The highest correlation is related to small lead times ($T \leq 15$ days).

We used the ROC diagram to determine the discrimination between active and inactive events of the MJO. We associated

255　1 to active MJO event and zero to the inactive events. In Figure 5, we show the ROC diagram for the different lead times T from 3 to 40 days. Analyzing the AUC, shown in Table 1, we find that until 40 days, the SWG is able to separate non-events (inactive MJO) from events as the AUC values are between 0.88 and 0.61. It is still significant as it is over the diagonal (random forecast). We notice that the sensitivity value is 0.9 for 3 days, and it decreases with lead time to reach 0.7 by 40 days. We also find that the specificity and sensitivity are equal for small lead times. However, the specificity remains above ≈ 0.5 for

260　$T = 40$ days. This value of specificity is still higher than ($1 - sensitivity = 0.2$). This indicates that the forecast has skill to distinguish between MJO events until 40 days ahead.

Table 1. Area under ROC curve (AUC) for the different lead times T from 3 to 40 days

T	3 days	5 days	10 days	20 days	30 days	40 days
AUC	0.88	0.83	0.74	0.66	0.62	0.61

Using three probabilistic metrics (CRPSS, correlation and ROC), we show that the SWG is able to skillfully forecast the MJO amplitude from analogs of Z500. The CRPSS shows a positive improvement of the forecast until 40 days. However, the correlation is significant until 20 days. By using the ROC curve and the discrimination skill, we show that the forecast still has

265　skill until 40 days.

The difference between the lead times that we found using the CRPSS, correlation and the ROC result from the difference between the skill scores. In fact, the CRPS is used for different categories of events, while the ROC is used for binary events, which is more suitable with our case of study.
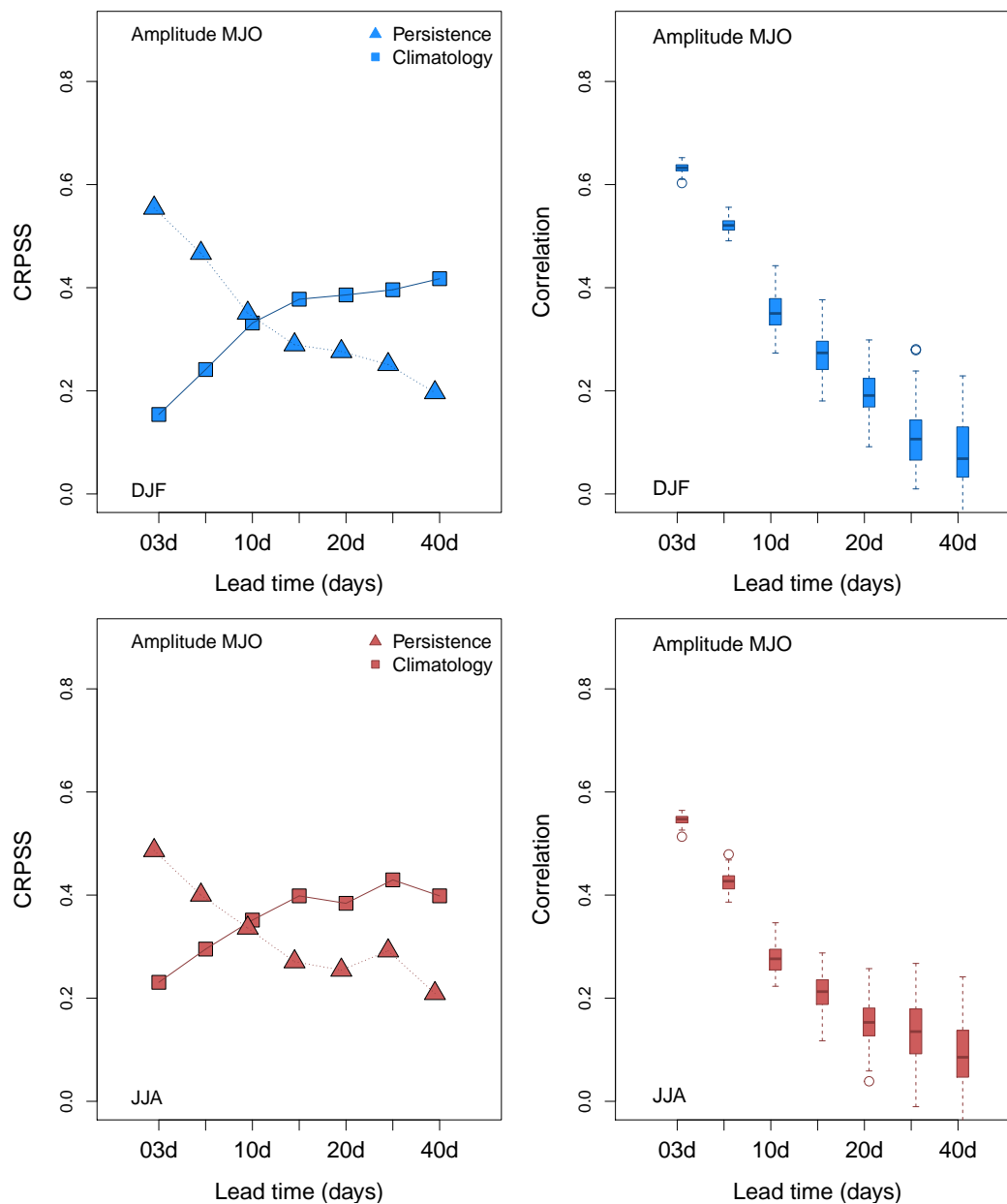
Figure 4. Skill scores for the MJO Amplitude for lead times going from 3 to 40 days for DJF (blue) and JJA (red) for analogs computed from Z500. Squares indicate CRPSS where the Persistence is the reference, triangles indicates CRPSS where the climatology is the reference, and box-plots indicates the probability distribution of correlation between observation and the median of 100 simulations for the period from 1979 to 2020.
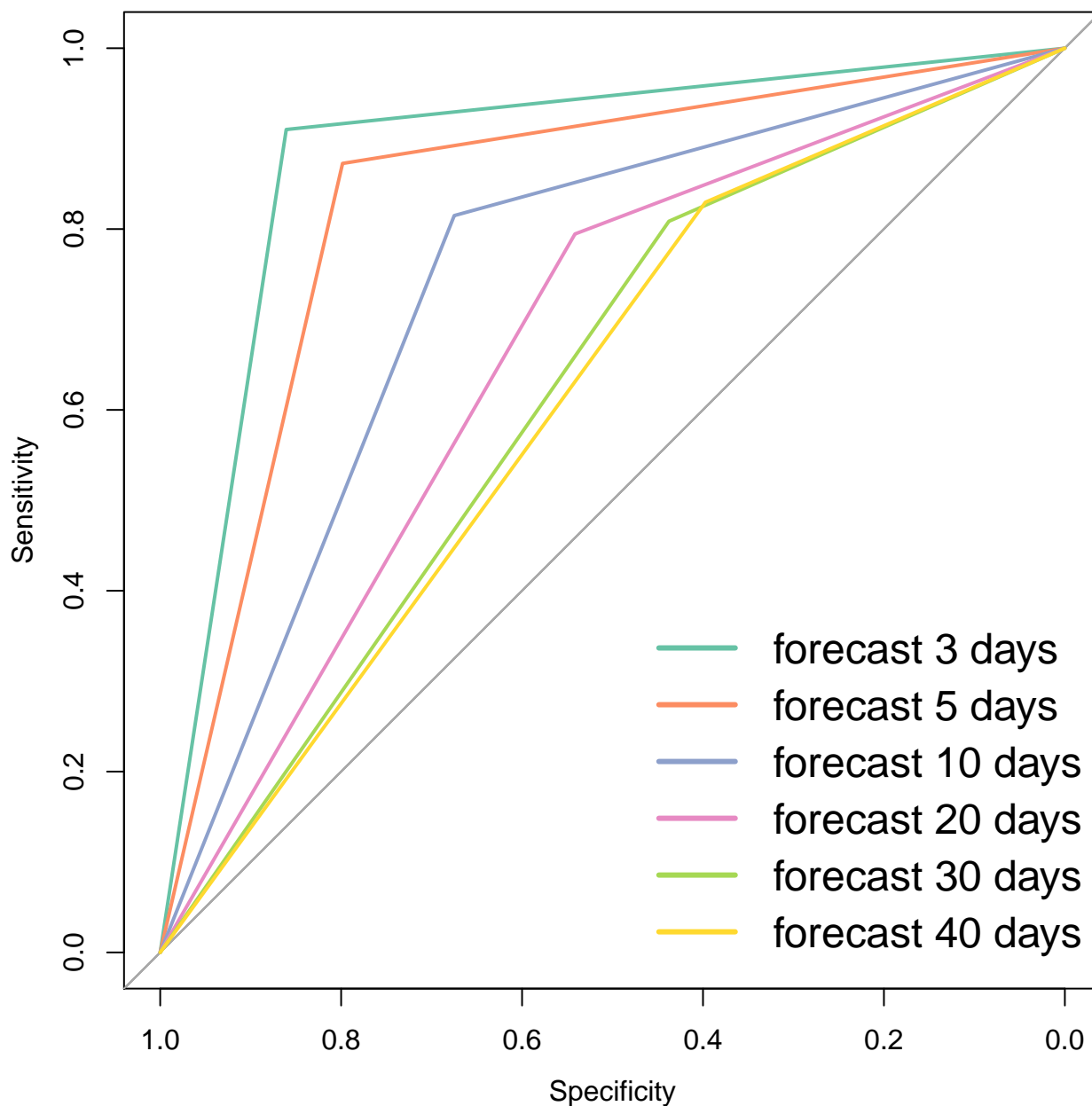
Figure 5. ROC curve for all lead times. The plot represents the sensitivity versus the specificity. The diagonal line represents the random classifier obtained when the forecast has no skill. If the ROC curve is below the diagonal line, then the forecast has a poor skill, otherwise it has a good skill, i.e. the forecast has the potential to distinguish between success and false alarm.

5.2 Evaluation of the Ensemble mean forecast of RMMs

270 In this part, we evaluate the performance of the SWG to forecast the RMMs (R_1 and R_2). We simulated R_1 and R_2 using the
SWG and analogs of Z500. Then we used the ensemble mean of R_1 and R_2 to compute the verification metrics mainly the
COR and RMSE (Rashid et al., 2011; Kim et al., 2018; Silini et al., 2021), as shown in Figure 6. We looked at COR and RMSE
averaged up to each lead time T. Respecting the threshold 0.5 for the COR and $\sqrt{2}$ for RMSE, we found that the forecast has
skill until $T = 40$ days. We have to mention that T of 60 and 90 days were used for verification purposes.
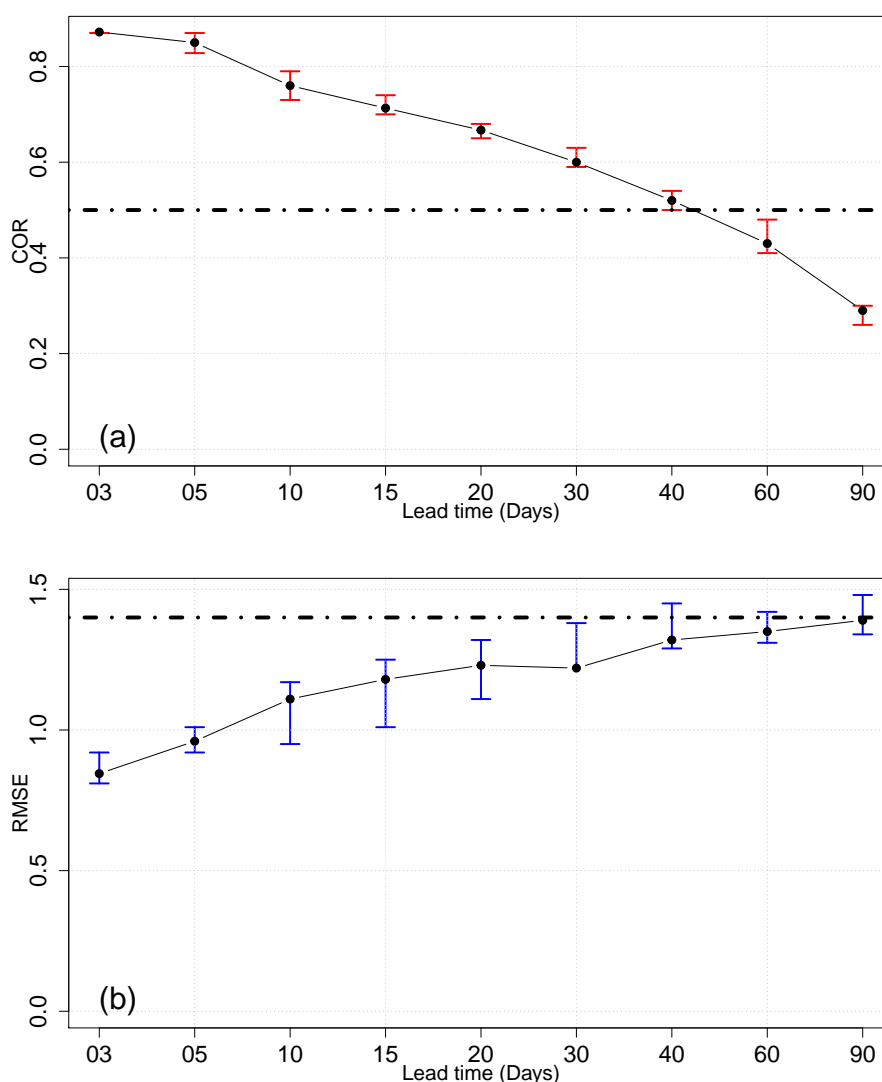
Figure 6. The COR and RMSE, respectively (a) and (b), for the different lead time of forecast from 3 days to 90 days over the period from
1979 to 2020. Confidence intervals are obtained with a bootstrap with 1000 samples.

16

275   In order to verify the forecast skill, we computed the ensemble spread and we compared it to the RMSE values for the different lead times going from 3 to 40 days (Figure 7). We found that the difference between the ensemble spread and the RMSE is increasing with lead time. The RMSE is becoming larger with lead time, which indicates that the distance between the observations and simulations is increasing. In addition, the ensemble spread is decreasing, which indicates that the uncertainties are increasing with time. This was verified by computing the bias of the forecast, where we could find that it is increasing with

280   lead time.
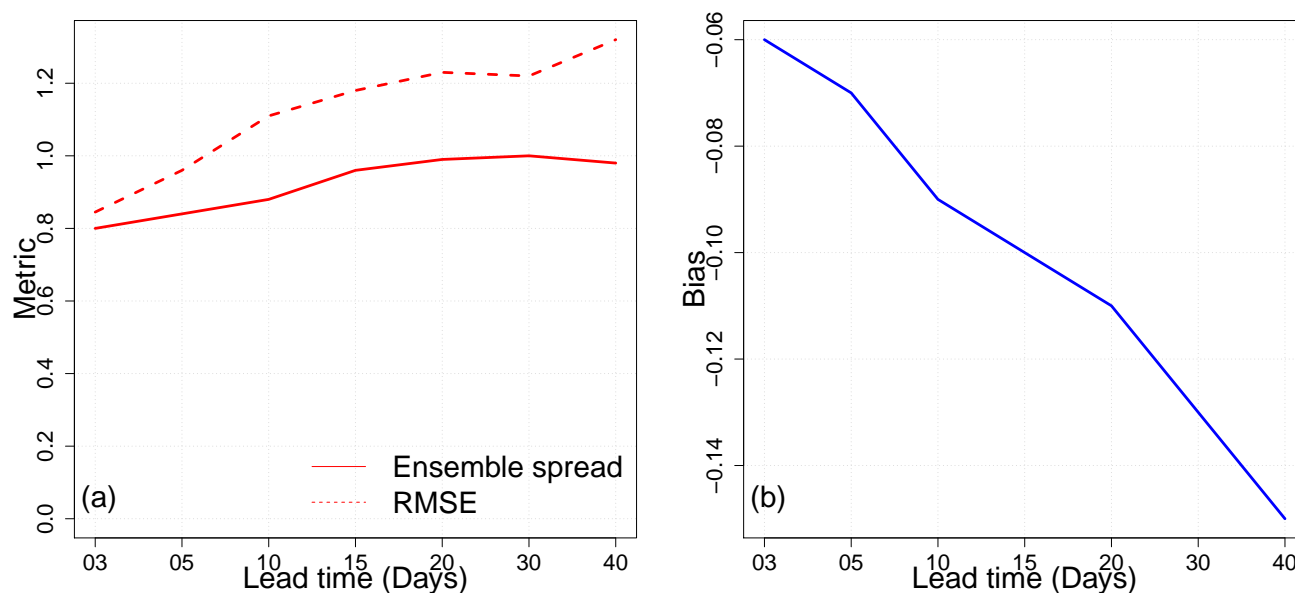
Figure 7. (a) Comparison between the ensemble spread and the RMSE. We notice that the difference is small for short lead times (≤ 15 days). "Metric" in the vertical axes refers to Ensemble spread and RMSE. (b) The bias between the simulations and the observations for the lead time going from 3 to 40 days.

We explored the sensitivity of the forecast to seasons as shown in Figure 8. We found that the forecast for DJF and MAM (March, April, May) has a good skill (i.e., with RMSE lower than $\sqrt{2}$) within 30 days. However, for SON (September, October and November) and JJA, the a similar forecast skill was obtained for a lead time of 40 days. The DJF and MAM seasons show the largest RMSE values. This indicates that the spread of the forecast is larger in DJFM than SON and JJA, even if the

285   observations and simulations are well correlated. The highest correlation on DJF and MAM could be explained by the fact that the MJO is more active in the boreal winter (DJFM). However, the RMSE values of JJA are more consistent as they represent low distance between simulations and observations. Indeed, even if the MJO events tend to be more intense in DJFM, the amplitude is underestimated. The assessment of the ensemble mean forecast of R1 and R2 showed that the forecast has skill until 40 days. However, it is sensitive to seasons and that is consistent with previous studies of Wheeler and Hendon (2004);

290   Rashid et al. (2011); Wu et al. (2016b). Indeed, we found that the SWG forecast of R1 and R2 has skill, with respect to the thresholds of COR and RMSE, within 40 days for summer (JJA) and 30 days for winter (DJF).
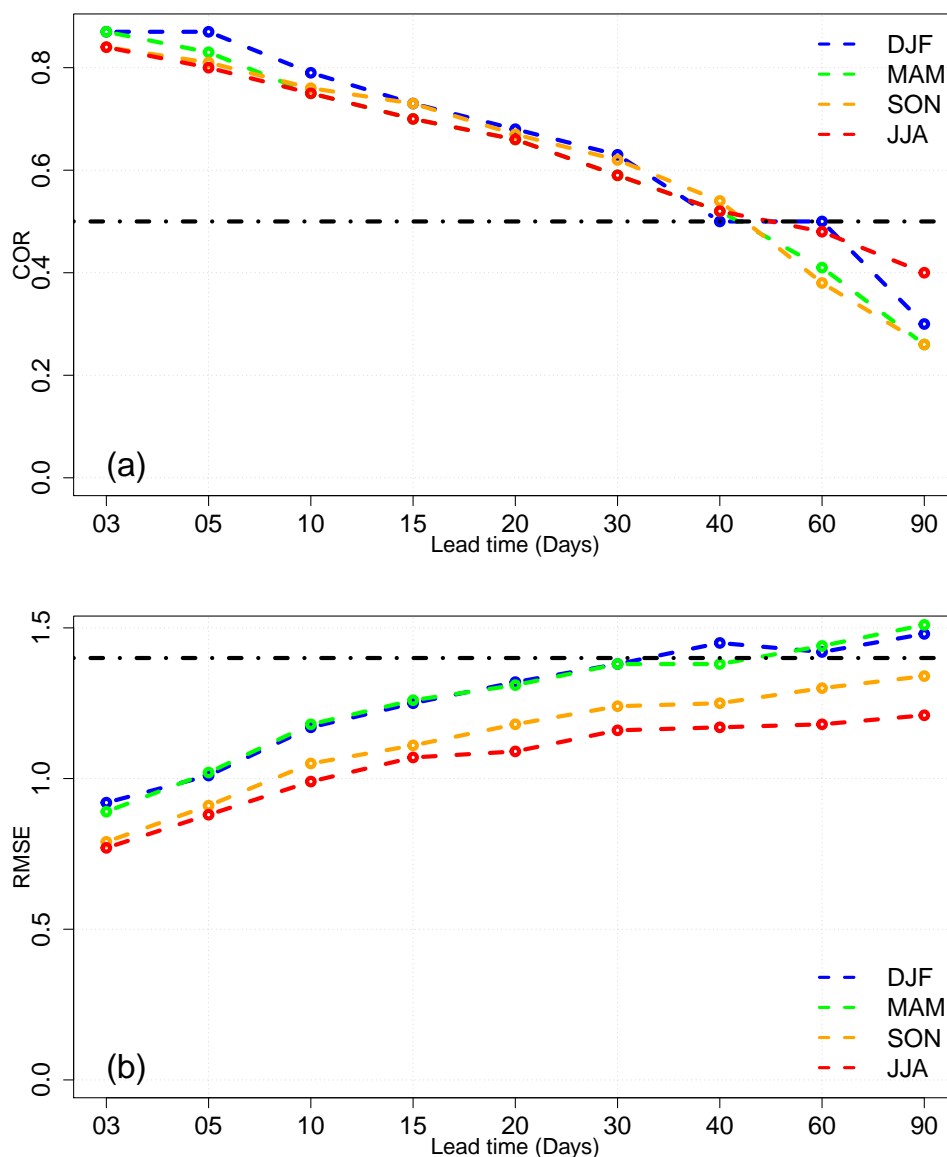
Figure 8. The COR and RMSE, respectively (a) and (b), for the different lead time of forecast from 3 days to 90 days over the period from 1979 to 2020 for the different seasons DJF, JJA, MAM and SON.

We also computed the amplitude and phase errors (Figure 9). We found that the $E_{A(t)}$ is negative for all lead times. That indicates a weak amplitude in predictions compared to the observations. The $E_{\phi(t)}$ is positive until 30 days, which indicates

fast propagation of the phase in predictions compared to the observations. Then it becomes negative, which means that the

295 phase is slower. We notice that the phase is well predicted while the amplitude is underestimated Figure 9. This is consistent

with previous studies (Silini et al., 2021; Rashid et al., 2011).
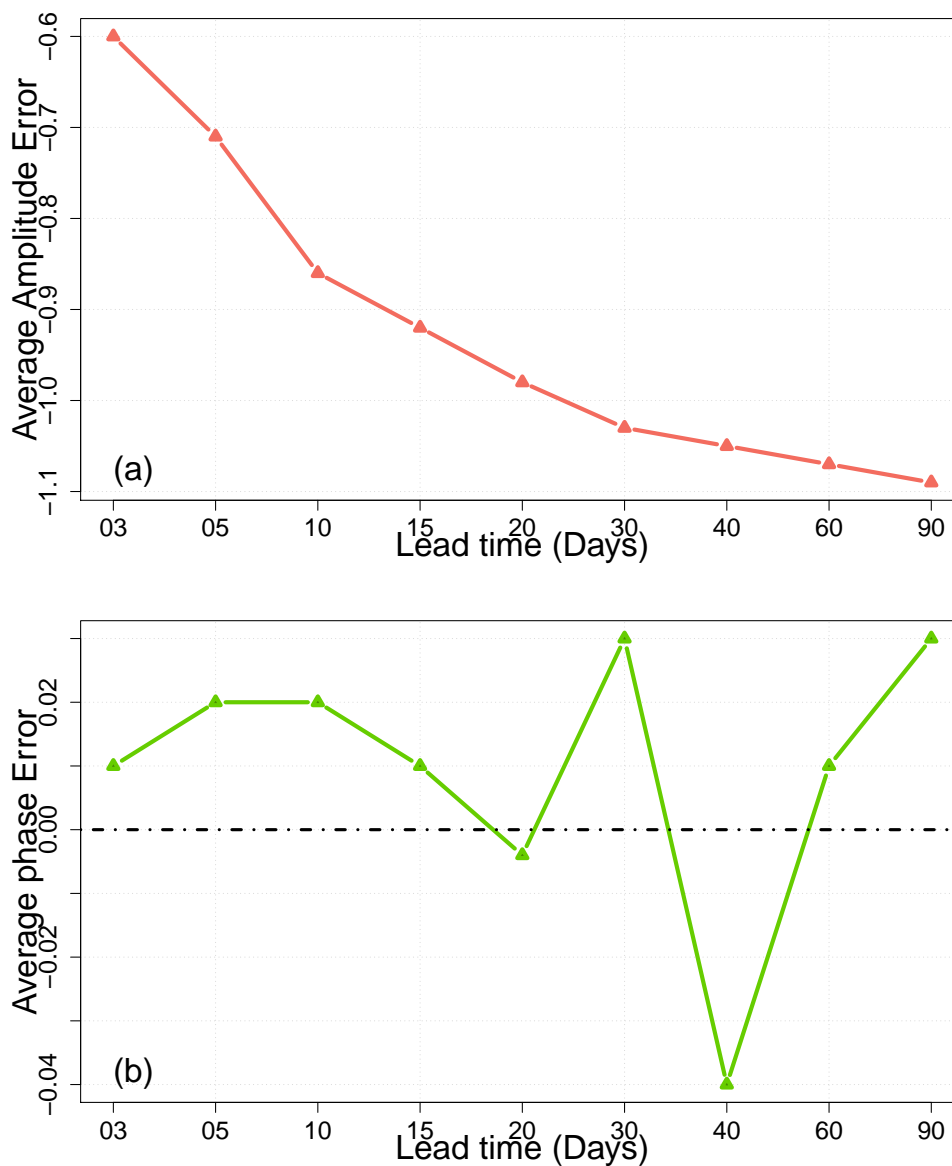
Figure 9. MJO Amplitude and phase average errors over all seasons for the period from 1979 to 2020. We notice that the amplitude is underestimated and the phase is well predicted by comparing predictions to forecast.

6 Comparison of the SWG forecast with other forecasts

The assessment of the forecast of MJO amplitude with SWG and analogs of Z500 shows good skill until 40 days using probabilistic scores (CRPSS vs. climatology is 0.2 and CRPSS vs. Persistence is 0.4) and scalar scores ($COR = 0.54$ and $RMSE = 1.30$) as explained in sections 5.1 and 5.2. The SWG forecast shows a positive improvement compared to the climatology and the persistence within 40 days Figure 4. In addition, the ROC curve confirmed the ability of the SWG forecast to distinguish between the active and inactive MJO amplitude as shown in Figure 5. The same result was obtained using the ensemble mean of RMM1 and RMM2 as represented in Figure 6. The SWG forecast of RMM1 and RMM2 has good skill within $30 - 40$ days respecting the threshold of 0.5 for the COR and $\sqrt{2}$ for RMSE. The difference on the lead time of the forecast depends on the seasons as represented in figure 8. This is consistent with Wu et al. (2016a); Wheeler and Weickmann (2001); Rashid et al. (2011), where they found significant differences between seasons. We found that the forecast has skill until 30 days for DJF and MAM (with $RMSE = \sqrt{2}$) and 40 days for JJA and SON (with $COR = 0.5$) Figure 8. This is different from Rashid et al. (2011) and Silini et al. (2021) who obtain higher forecast skill in the winter. However, it is in accordance with results of Wu et al. (2016b) who found better skills for JJA.

We assessed the forecast skill of the SWG with other forecast. We selected two models POAMA (the Australian Bureau of Meteorology coupled ocean-atmosphere seasonal prediction system) and ECMWF, which are providing respectively probabilistic and deterministic forecast of the MJO. We compared mainly the maximum lead time of the MJO amplitude forecast. The POAMA model provides 10-member ensemble. In hindcast mode, the POAMA model has skill up to 21 days (Rashid et al., 2011). The ECMWF reforecasts with Cycle 46r1 has skill to around 40 days. For the error of the amplitude and phase, we found that ECMWF reforecast shows lower amplitude and phase averaged errors compared to those from the SWG forecasts. However, what we found is consistent with other dynamical models (Kim et al., 2018) where they overestimate or underestimate the amplitude and the phase of the MJO.

In addition, we compared quantitatively the SWG forecast with the ECMWF forecast Figure 10. The ECMWF reforecats were taken from (Silini et al., 2022). We found that the ECMWF forecast has highest correlation until 20 days compared to the SWG forecast. The RMSE values of ECMWF forecast are always small compared to the SWG forecast, which indicates a good reliability skill of the ECMWF forecast for lead times of 5 and 10 days. However, for lead times of 20 days the RMSE of ECMWF forecast coincides with the RMSE of the SWG, which shows the improvement of the SWG forecast to lead time above 20 days. The skill scores of the ECMWF (COR and RMSE) (Silini et al., 2022) are computed for each lead time, which is different from our way of computing the skill score (considering the average lead time). Of course, this comparison was made to check the performance of our forecast and not to say that the SWG model can replace a numerical prediction.

We also compared the SWG forecast skill with a machine learning forecast of MJO indices (RMM1 and RMM2) (Silini et al., 2021) . Silini et al. (2021) explored the skill forecast of two artificial neural network types, FFNN (feed-forward neural network) and the AR-RNN (autoregressive recurrent neural network) on MJO indices. Silini et al. (2021) found that the machine learning method gives good skill scores until $26 - 27$ days with respect to the standard thresholds of COR and RMSE. We compared the skill scores (RMSE and COR) of the SWG and Silini et al. (2021) forecasts for all lead times. We found that the two models

have the same correlation until 10 days. After 10 days, the correlation of Silini et al. (2021) forecasts decreases rapidly while the correlation of SWG is still significant. For the RMSE, we found that the SWG has smaller values for lead time of 10 days. This indicates that the SWG forecast is more reliable. However, from 30 days, the RMSE of the two models starts to be the same.

335   To sum up, the comparison of SWG forecast to ECMWF and Silini et al. (2021) forecasts shows that for small lead time (up to 10 days) the ECMWF forecast has better skill. However, the SWG shows positive improvement for long lead times.
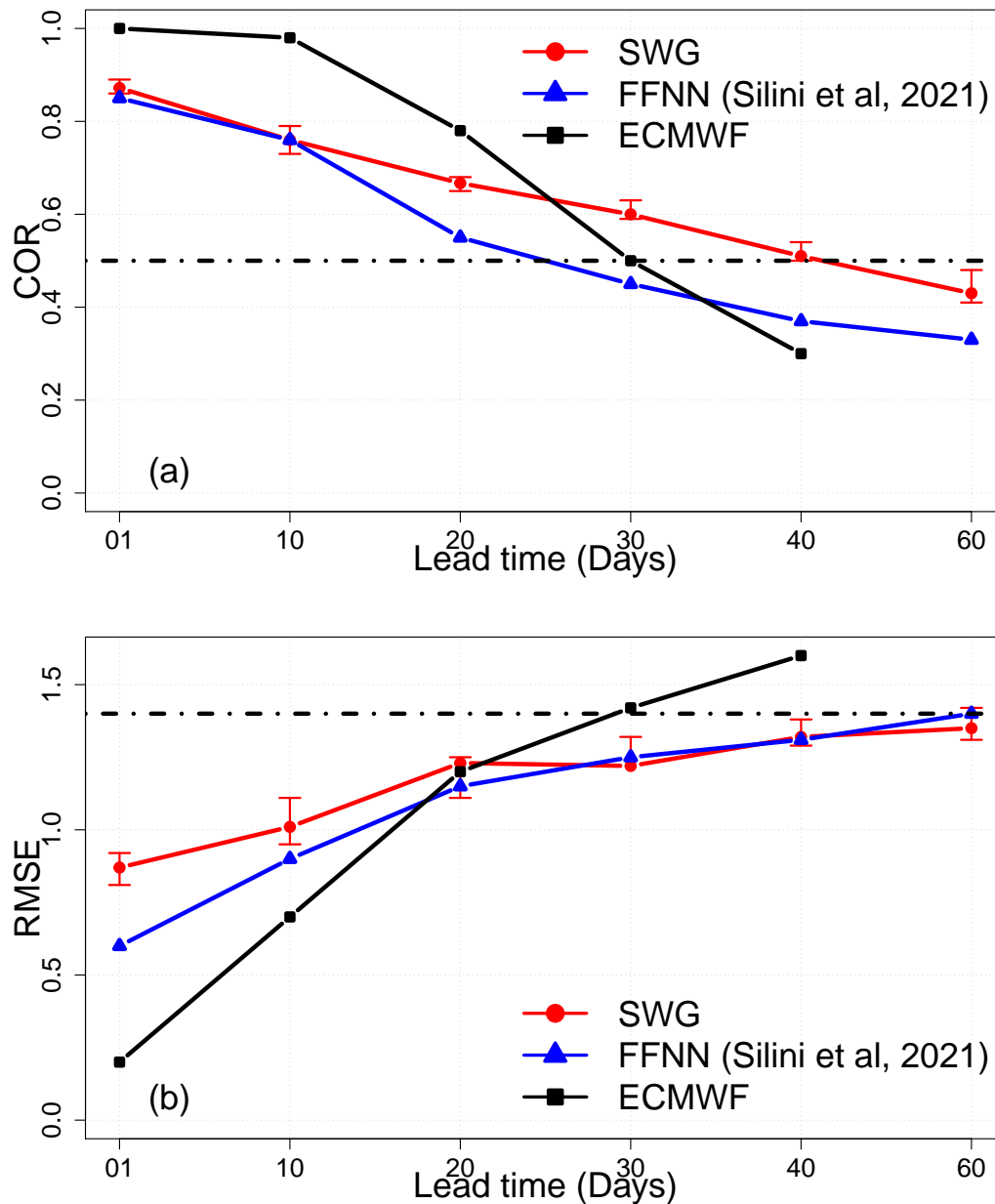
Figure 10. Comparison of the values of COR (a) and RMSE (b) between the SWG forecast and forecasts of Silini et al. (2021) (blue lines) and ECMWF (black lines). Confidence intervals for SWG (red lines) were obtained by with a bootstrap procedure over the simulations (1000 samples).

7 Conclusions

We performed an ensemble forecast of the MJO amplitude using analogs of the atmospheric circulation and a stochastic weather generator. We used the Z500 as a driver of the circulation over the Indian ocean and we considered analogs from the same phase to do the forecast. We explored two ways to forecast the MJO, starting by forecasting directly the daily amplitude, then the daily MJO indices, RMM1 and RMM2, from 1979 to 2020.

We assessed the forecast skill of the MJO forecast by evaluating the ensemble member and the mean of the ensemble member, using respectively probabilistic and scalar verification methods. This allowed us to evaluate the forecast and also to explore the difference between the two verification methods.

We used probabilistic skill scores as the CRPSS and the ROC. We found that the forecast is good within 40 days. Using the scalar scores (COR and RMSE) and the ensemble mean of the forecast of RMM1 and RMM2, we found that the SWG is able to forecast the MJO indices (RMM1 and RMM2) within 30 – 40 days.

We found that the forecast is sensitive to seasons. The forecast has skill up to 30 days for the boreal winter (DJF and MAM), while it goes to 40 days for the boreal summer (JJA) and SON. That was consistent with previous studies (Silini et al., 2021; Rashid et al., 2011). We also notice that the forecast of the phase is better than of the amplitude. Finally, we find that the SWG had improvement over the ECMWF and a maachine learning (Silini et al., 2021) forecasts, especially for long lead times.

This paper hence confirms the skill of the SWG to generate ensembles of MJO indices forecasts from analogs of circulation. Such information would be useful to forecast impact variables such as precipitation and temperature.

Code availability. The code and data files are available at http://doi.org/10.5281/zenodo.4524562

Appendix A: Comparison of the forecast skill of the MJO using analogs computed from Z500, Z300 and OLR fields

360   We did the forecast of RMM1 and RMM2 using analogs of Z300 (Figure A5) and OLR (Figure A4). We found that the model yields good skills ($COR > 0.5$ and $RMSE < 1.4$) until $T = 60$ days (Figure A1). However, the skill of the forecast is better for small lead times ≤ 30 days with Z500 (Figure A1). We checked the sensitivity of the forecast to seasons (Figures A3 and A2).
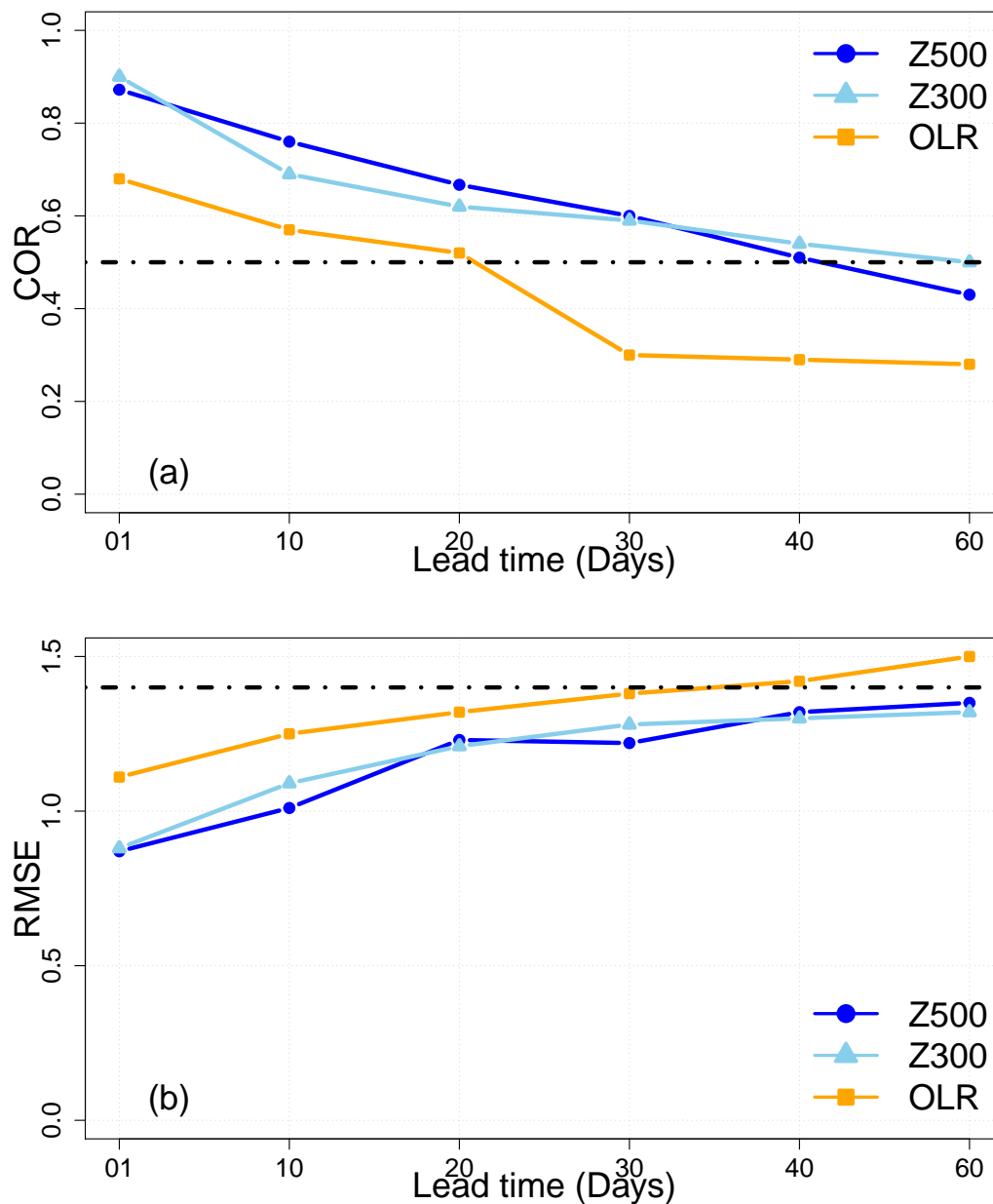
Figure A1. COR (panel a) and RMSE (panel b) values for different lead time of forecast from 3 days to 90 days over the period from 1979 to 2020 with analogs of Z300 and Z500.
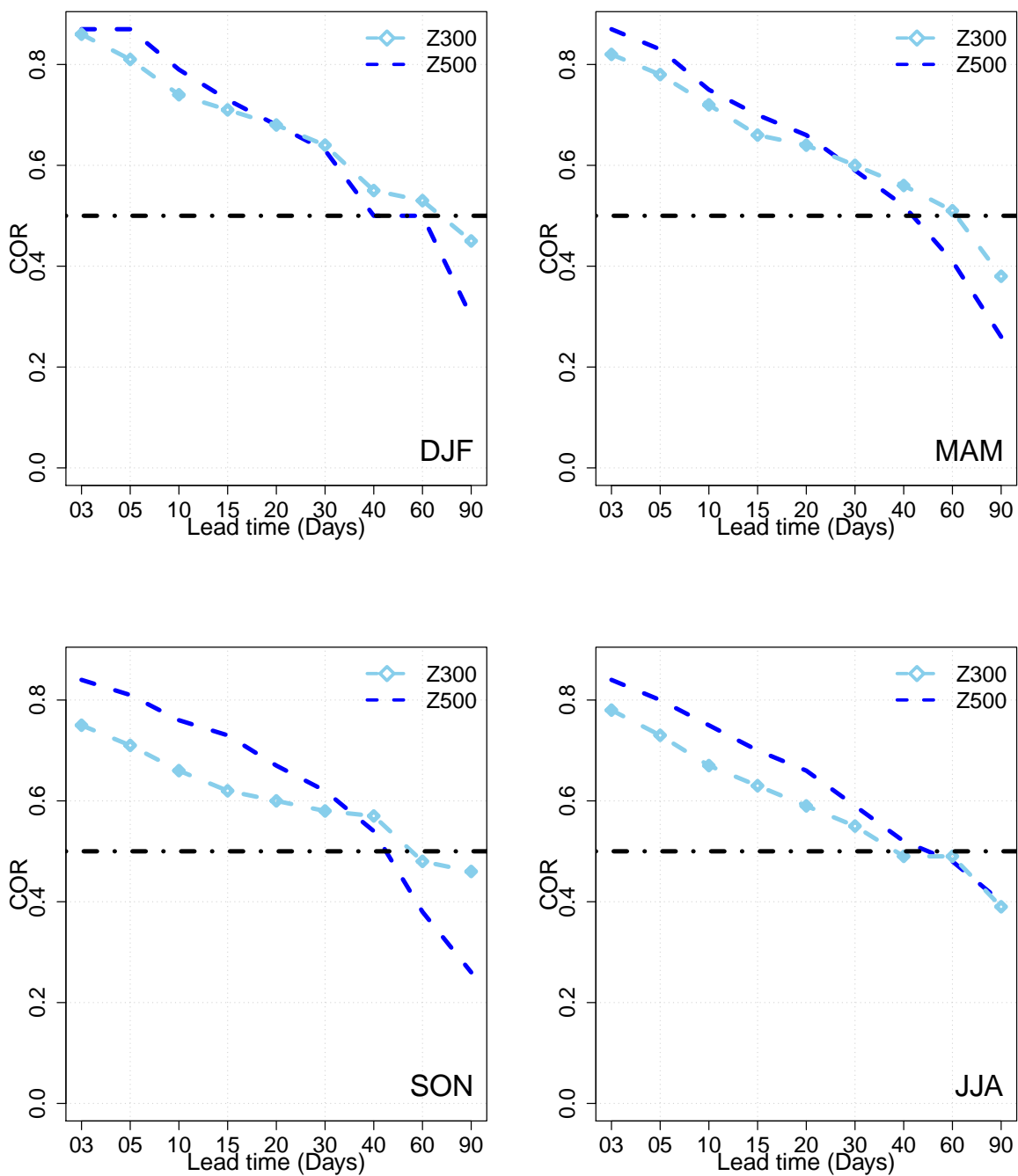
Figure A2. COR values for different lead times of forecast from 3 days to 90 days over the period from 1979 to 2020 for the different seasons (DJF, JJA, MAM and SON).
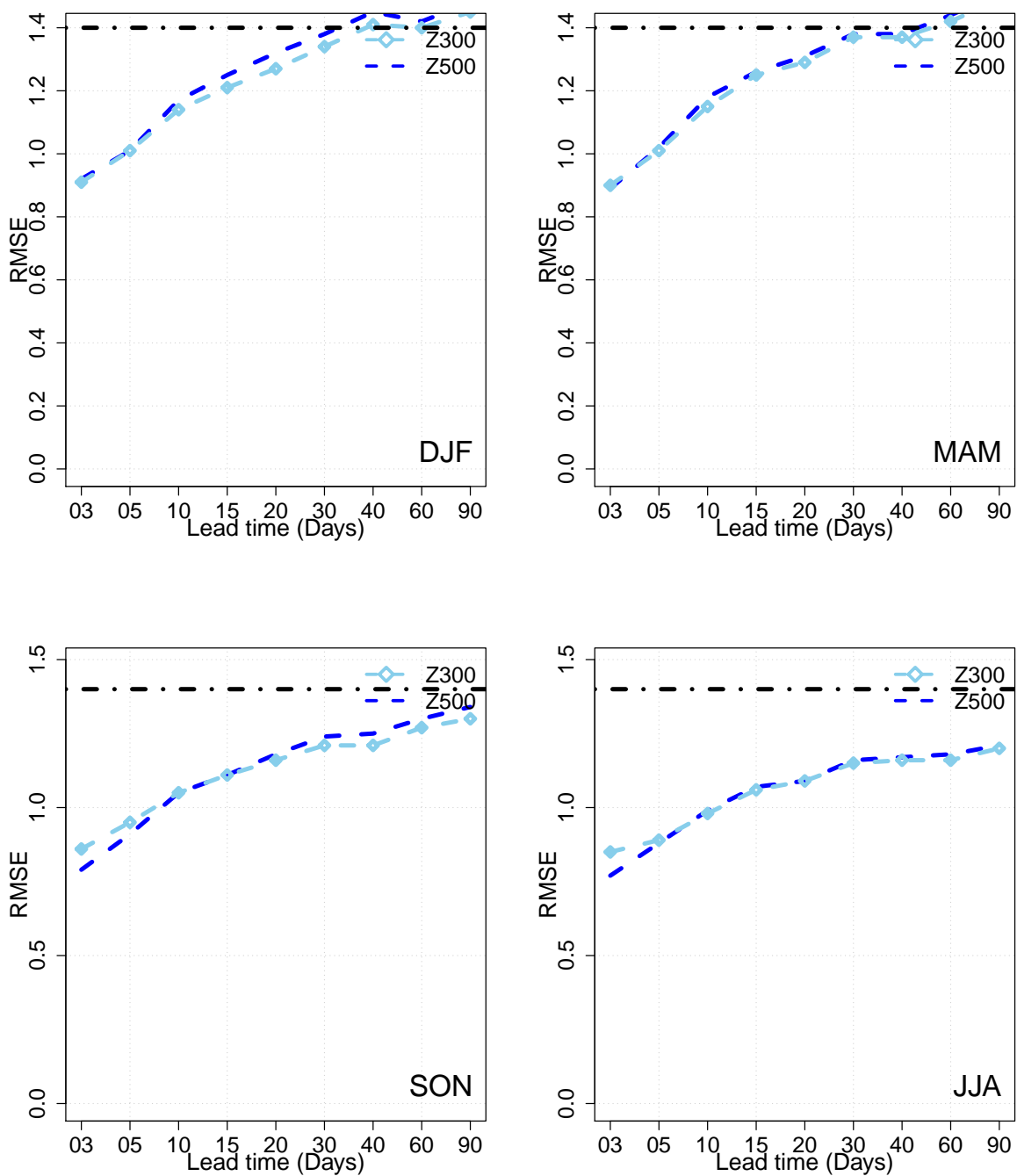
Figure A3. RMSE values for different lead times of forecast from 3 days to 90 days over the period from 1979 to 2020 for the different seasons (DJF, JJA, MAM and SON).
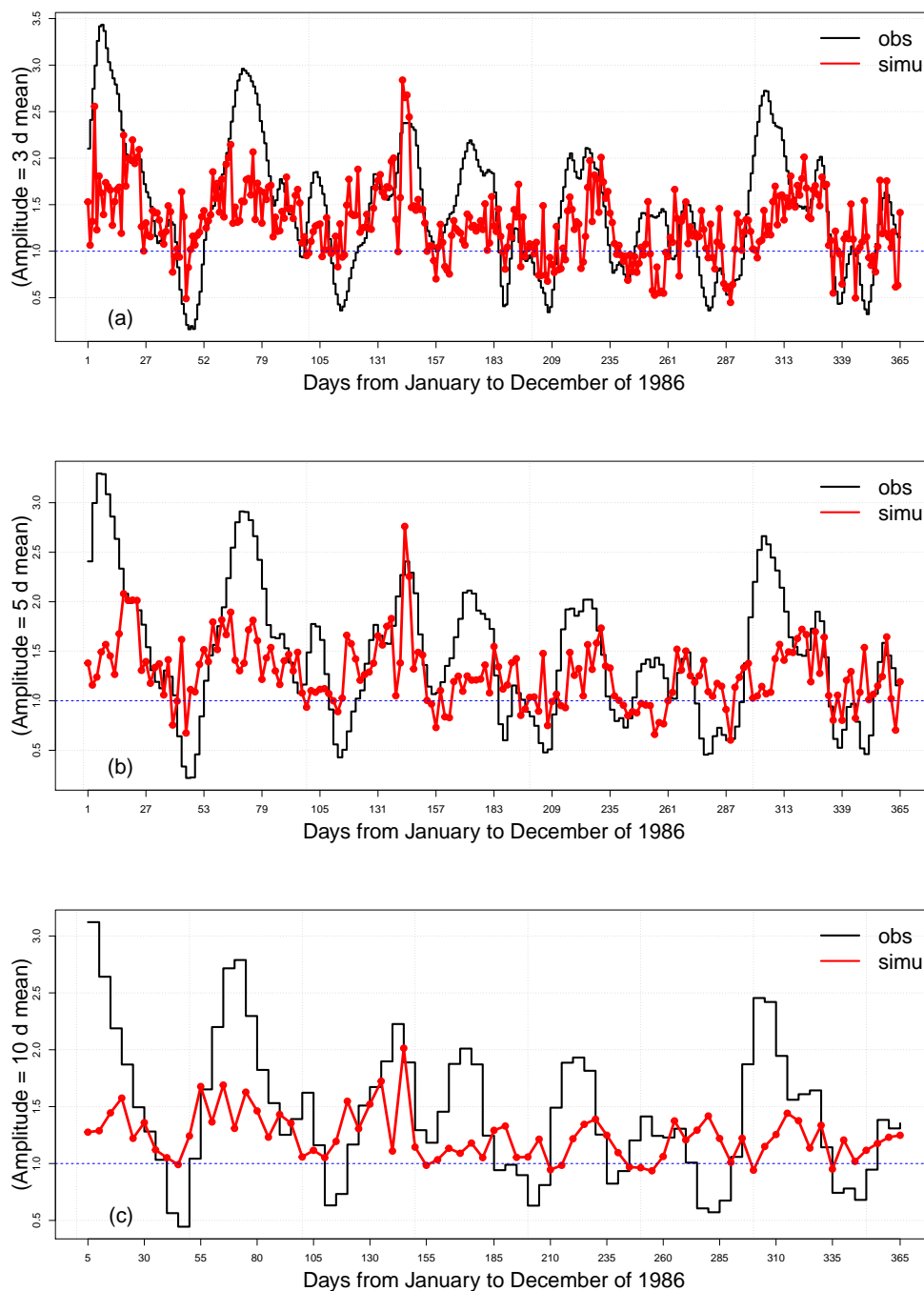
Figure A4. Time series of observations and simulations of the MJO Amplitude computed from analogs of OLR, for lead time of 3, 5 and 10 days, respectively (a), (b) and (c), for the year 1986. The red line represents the mean of the 100 simulations, the black line represents the observations, and the blue line indicates the threshold of the MJO activity.
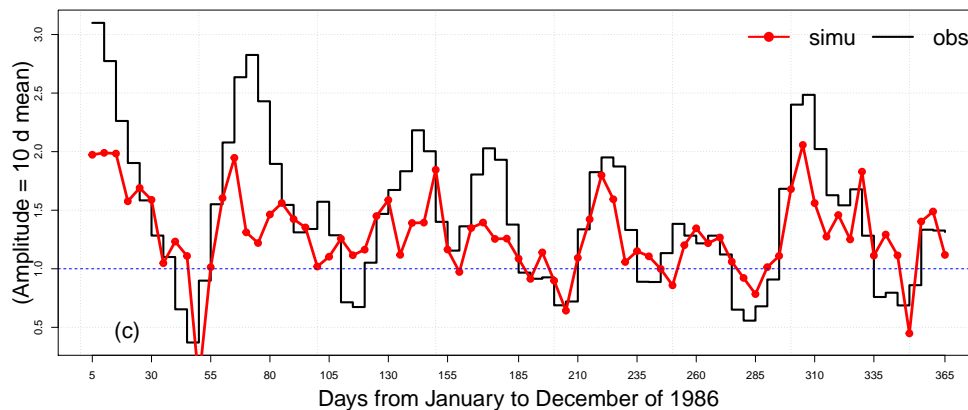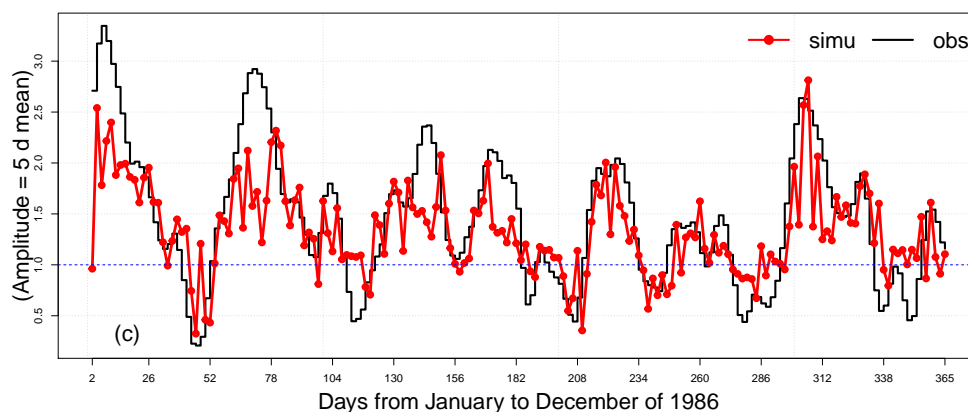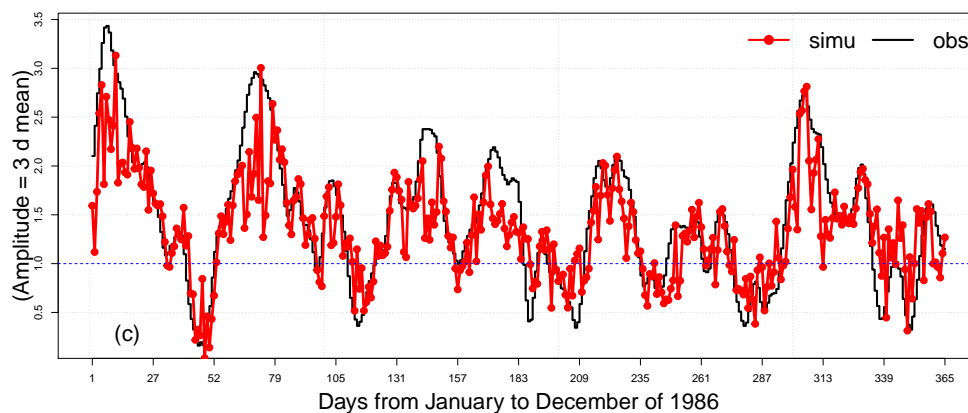
Figure A5. Time series of observations and simulations of the MJO Amplitude computed from analogs of Z300, for lead time of 3, 5 and 10 days, respectively (a), (b) and (c), for the year 1986. The red line represents the mean of the 100 simulations, the black line represents the observations, and the blue line indicates the threshold of the MJO activity.

We compared the CRPS and the RMSE (computed between the mean of the simulations and the observations) for different

365   lead times. We found that the RMSE values for the forecast based on analogs of the OLR are slightly higher than the RMSE values for the forecast based on analogs of Z500.

Appendix B: Domains of computation of analogs
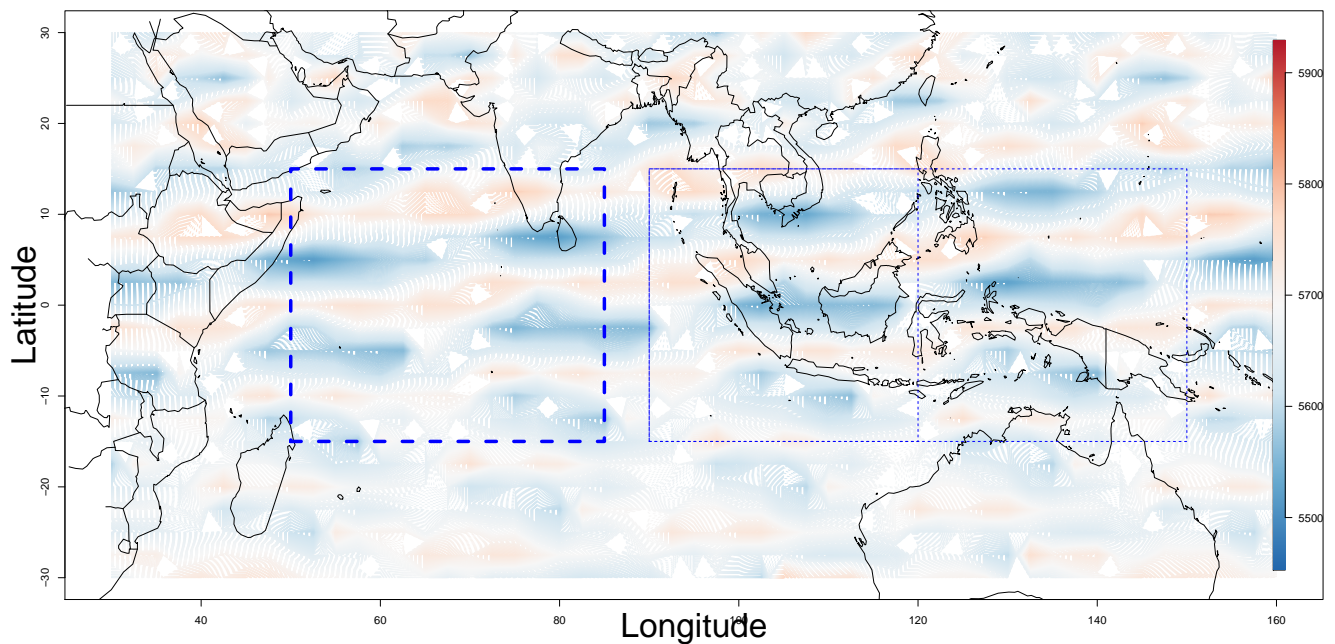
Figure B1. Domains of computation of analogs, we computed analogs over the Indian ocean with coordinates (50E, 85E – 15S,15N), the Indian-Pacific ocean with coordinates (85E, 120E – 15S,15N) and the Indian-maritime ocean with coordinates (120E, 170E – 15S,15N).

References

Ailliot, P., Allard, D., Monbet, V., and Naveau, P.: Stochastic weather generators: an overview of weather type models, Journal de la Société
370   Française de Statistique, p. 15, 2015.

Atencia, A. and Zawadzki, I.: A comparison of two techniques for generating nowcasting ensembles. Part I: Lagrangian ensemble technique,
      Monthly Weather Review, 142, 4036–4052, 2014.

Barlow, M., Zaitchik, B., Paz, S., Black, E., Evans, J., and Hoell, A.: A Review of Drought in the Middle East and Southwest Asia, Journal
      of Climate, 29, 8547 – 8574, https://doi.org/10.1175/JCLI-D-13-00692.1, 2016.

375   Becker, E. J., Berbery, E. H., and Higgins, R. W.: Modulation of Cold-Season U.S. Daily Precipitation by the Madden–Julian Oscillation, J.
      Climate, 24, 5157–5166, https://doi.org/10.1175/2011JCLI4018.1, 2011.

Blanchet, J., Stalla, S., and Creutin, J.-D.: Analogy of multiday sequences of atmospheric circulation favoring large rainfall accumulation
      over the French Alps, Atmos. Sci. Lett., 19, e809, https://doi.org/10.1002/asl.809, 2018.

Cassou, C.: Intraseasonal interaction between the Madden–Julian Oscillation and the North Atlantic Oscillation, Nature, 455, 523–527,
380   https://doi.org/10.1038/nature07286, 2008.

Fawcett, T.: An introduction to ROC analysis, Pattern Recognition Letters, 27, 861–874, https://doi.org/10.1016/j.patrec.2005.10.010, 2006.

Grimit, E. P. and Mass, C. F.: Initial Results of a Mesoscale Short-Range Ensemble Forecasting System over the Pacific Northwest, Weather
      and forecasting, 17, 192–205, https://doi.org/10.1175/1520-0434(2002)017<0192:IROAMS>2.0.CO;2, 2002.

Hersbach, H.: Decomposition of the Continuous Ranked Probability Score for Ensemble Prediction Systems, WEATHER AND FORE-
385   CASTING, 15, 12, 2000.

Hersbach, H., Bell, B., Berrisford, P., Hirahara, S., Horányi, A., Muñoz-Sabater, J., Nicolas, J., Peubey, C., Radu, R., and Schepers, D.: The
      ERA5 global reanalysis, Quat. J. Roy. Met. Soc., 146, 1999–2049, 2020.

Kim, H., Vitart, F., and Waliser, D. E.: Prediction of the Madden–Julian Oscillation: A Review, J. Climate, 31, 9425–9443,
      https://doi.org/10.1175/JCLI-D-18-0210.1, 2018.

390   Kistler, R., Kalnay, E., Collins, W., Saha, S., White, G., Woollen, J., Chelliah, M., Ebisuzaki, W., Kanamitsu, M., Kousky, V., van den
      Dool, H., Jenne, R., and Fiorino, M.: The NCEP-NCAR 50-year reanalysis: Monthly means CD-ROM and documentation, Bulletin of the
      American Meteorological Society, 82, 247–267, <GotoISI>://000166742900003, 2001.

Krouma, M., Yiou, P., Déanderis, C., and Thao, S.: Assessment of stochastic weather forecast based on analogues of circulation, Geoscientific
      Model Development, p. 17, 2021.

395   Lafleur, D. M., Barrett, B. S., and Henderson, G. R.: Some Climatological Aspects of the Madden–Julian Oscillation (MJO), Journal of
      Climate, 28, 6039–6053, https://doi.org/10.1175/JCLI-D-14-00744.1, 2015.

Lim, Y., Son, S.-W., and Kim, D.: MJO Prediction Skill of the Subseasonal-to-Seasonal Prediction Models, Journal of Climate, 31, 4075–
      4094, https://doi.org/10.1175/JCLI-D-17-0545.1, 2018.

Lin, H., Brunet, G., and Derome, J.: Forecast Skill of the Madden–Julian Oscillation in Two Canadian Atmospheric Models, Monthly Weather
400   Review, 136, 4130 – 4149, https://doi.org/10.1175/2008MWR2459.1, 2008.

Lorenz, E. N.: Atmospheric Predictability as Revealed by Naturally Occurring Analogues, J. Atmos. Sci., 26, 636–646, 1969.

Marshall, A. G., Hendon, H. H., and Hudson, D.: Visualizing and verifying probabilistic forecasts of the Madden-Julian Oscillation: PROB-
      ABILISTIC MJO FORECASTS, Geophys. Res. Lett., 43, 12,278–12,286, https://doi.org/10.1002/2016GL071423, 2016.

Palmer, T. N.: Predicting uncertainty in forecasts of weather and climate, Reports on Progress in Physics, 63, 71–116, <GotoISI>:
//000085479700001, 2000.

Pegion, K. and Kirtman, B. P.: The Impact of Air–Sea Interactions on the Predictability of the Tropical Intraseasonal Oscillation, Journal of
Climate, 21, 5870–5886, https://doi.org/10.1175/2008JCLI2209.1, 2008.

Platzer, P., Yiou, P., Naveau, P., Filipot, J.-F., Thiébaut, M., and Tandeo, P.: Probability Distributions for Analog-To-Target Distances, Journal
of the Atmospheric Sciences, 78, 3317 – 3335, https://doi.org/10.1175/JAS-D-20-0382.1, 2021.

Rashid, H. A., Hendon, H. H., Wheeler, M. C., and Alves, O.: Prediction of the Madden–Julian oscillation with the POAMA dynamical
prediction system, Clim Dyn, 36, 649–661, https://doi.org/10.1007/s00382-010-0754-x, 2011.

Scaife, A. A., Arribas, A., Blockley, E., Brookshaw, A., Clark, R. T., Dunstone, N., Eade, R., Fereday, D., Folland, C. K., and Gordon, M.:
Skillful long-range prediction of European and North American winters, Geophysical Research Letters, 41, 2514–2519, 2014.

Silini, R., Barreiro, M., and Masoller, C.: Machine learning prediction of the Madden-Julian oscillation, npj Clim Atmos Sci, 4, 57,
https://doi.org/10.1038/s41612-021-00214-6, 2021.

Silini, R., Lerch, S., Mastrantonas, N., Kantz, H., Barreiro, M., and Masoller, C.: Improving the prediction of the Madden-Julian Oscillation
of the ECMWF model by post-processing, EGUsphere, 2022, 1–15, https://doi.org/10.5194/egusphere-2022-2, 2022.

Sivillo, J. K., Ahlquist, J. E., and Toth, Z.: An ensemble forecasting primer, Weather and Forecasting, 12, 809–818, <GotoISI>:
//000071577700008, 1997.

Stachnik, J. P. and Chrisler, B.: An index intercomparison for MJO events and termination, Journal of Geophysical Research: Atmospheres,
125, e2020JD032 507, 2020.

Straub, K. H.: MJO Initiation in the Real-Time Multivariate MJO Index, Journal of Climate, 26, 1130–1151, https://doi.org/10.1175/JCLI-
D-12-00074.1, 2013.

Toth, Z. and Kalnay, E.: Ensemble forecasting at NCEP and the breeding method, MONTHLY WEATHER REVIEW, 125, 3297–3319,
<GotoISI>://A1997YJ55500014, 1997.

Ventrice, M. J., Wheeler, M. C., Hendon, H. H., Schreck, C. J., Thorncroft, C. D., and Kiladis, G. N.: A Modified Multivariate Mad-
den–Julian Oscillation Index Using Velocity Potential, Monthly Weather Review, 141, 4197–4210, https://doi.org/10.1175/MWR-D-12-
00327.1, 2013.

Verde, M. F.: Measures of sensitivity based on a single hit rate and false alarm rate: The accuracy, precision, and robustness of d , Az, and A,
Perception & Psychophysics, p. 12, 2006.

Wheeler, M. and Weickmann, K. M.: Real-Time Monitoring and Prediction of Modes of Coherent Synoptic to Intraseasonal Tropical Vari-
ability, Monthly Weather Review, 129, 2677 – 2694, https://doi.org/10.1175/1520-0493(2001)129<2677:RTMAPO>2.0.CO;2, 2001.

Wheeler, M. C. and Hendon, H. H.: An All-Season Real-Time Multivariate MJO Index: Development of an Index for Monitoring and
Prediction, MONTHLY WEATHER REVIEW, 132, 16, 2004.

Wu, J., Ren, H.-L., Zuo, J., Zhao, C., Chen, L., and Li, Q.: MJO prediction skill, predictability, and teleconnection impacts
in the Beijing Climate Center Atmospheric General Circulation Model, Dynamics of Atmospheres and Oceans, 75, 78–90,
https://doi.org/https://doi.org/10.1016/j.dynatmoce.2016.06.001, 2016a.

Wu, J., Ren, H.-L., Zuo, J., Zhao, C., Chen, L., and Li, Q.: MJO prediction skill, predictability, and teleconnection impacts
in the Beijing Climate Center Atmospheric General Circulation Model, Dynamics of Atmospheres and Oceans, 75, 78–90,
https://doi.org/https://doi.org/10.1016/j.dynatmoce.2016.06.001, 2016b.

Xiang, B., Zhao, M., Jiang, X., Lin, S.-J., Li, T., Fu, X., and Vecchi, G.: The 3–4-Week MJO Prediction Skill in a GFDL Coupled Model, Journal of Climate, 28, 5351–5364, https://doi.org/10.1175/JCLI-D-15-0102.1, 2015.

Yiou, P.: AnaWEGE: a weather generator based on analogues of atmospheric circulation, Geosci. Model Dev., 7, 531–543, https://doi.org/10.5194/gmd-7-531-2014, 2014.

445 Yiou, P. and Déandréis, C.: Stochastic ensemble climate forecast with an analogue model, Geosci. Model Dev., 12, 723–734, https://doi.org/10.5194/gmd-12-723-2019, 2019.

Zamo, M. and Naveau, P.: Estimation of the Continuous Ranked Probability Score with Limited Information and Applications to Ensemble Weather Forecasts, Mathematical Geosciences, 50, 209–234, 2018.

Zhang, C.: Madden–Julian Oscillation: Bridging Weather and Climate, Bull. Amer. Meteor. Soc., 94, 1849–1870,
450 https://doi.org/10.1175/BAMS-D-12-00026.1, 2013.

Zhang, C., Gottschalck, J., Maloney, E. D., Moncrieff, M. W., Vitart, F., Waliser, D. E., Wang, B., and Wheeler, M. C.: Cracking the MJO nut: ZHANG ET AL.: CRACKING THE MJO NUT, Geophys. Res. Lett., 40, 1223–1230, https://doi.org/10.1002/grl.50244, 2013.